A MAGNETOSPHERIC MAGNETIC FIELD MODEL
WITH A WARPED TAIL CURRENT SHEET

N. A. TSYGANENKO

Institute of Physics, Leningrad State University, Leningrad 198904, U.S.S.R.

Abstract—An improved quantitative representation of the magnetic field in the geomagnetosphere is developed. The model takes into account the effect of warping the tail current sheet in two dimensions due to the geodipole tilt, as well as spatial variations of the current sheet thickness along the Sun–Earth and dawn–dusk directions. The corresponding analytic forms for the magnetic field components have been obtained using an indirect approach in a two-stage procedure. First of all, a simple axially symmetric infinitely thin current disc model with different rates of the current density decreasing in the radial direction are derived. The next step consists in a formal modification of the obtained expressions for the vector potential, which results in a transverse broadening of the initially thin current sheet and incorporates an account for the sheet warping. A truncation factor is also introduced, with the aim to simulate the finite extension of the current system in the dawn-dusk direction, as well as its day–night asymmetry. Based on the proposed representation and the *IMP* and *HEOS* spacecraft data pool, a series of magnetospheric models are generated, giving a quantitative description of the average magnetic field configuration for different disturbance levels. A comparison of the magnetic field distributions predicted by the model and those measured at geosynchronous orbit has been carried out.

1. INTRODUCTION

It is well established that the region near the inner edge of the plasma sheet in the nightside magnetosphere plays a key role in the dynamics of disturbances. The structure of geomagnetic field and plasma in this region is extremely variable, since it is just here that the boundary between the "spheres of influence" of the Earth's internal field sources and the magnetotail currents, controlled by the solar wind, is located. Several experimental facts concerning this region can be pointed out, which should be taken into account in any quantitative model aimed at an adequate representation of the average magnetic field and current distribution. These are the following results.

(1) There exists strong evidence that an intense and thin current sheet can approach the Earth as close as 3–5 R_E at the nightside. This was suggested by Sugiura (1972) as a direct implication of the observed features of the ΔB distribution in the inner magnetosphere. Hedgecock and Thomas (1975) pointed out that the tail-like configuration is clearly discernible in the *HEOS* magnetic field data at tailward distances of 6–8 R_E, with the current sheet thickness less than 1 R_E. Lin and Barfield (1984) showed in a statistical study that the tail-like fields can often be observed at geosynchronous orbit in the mid-

night sector, with increasing probability during disturbed periods, and estimated the current sheet thickness to be of the order of several tenths of R_E. Kaufmann (1987) also addressed the question of tail-like magnetic configurations observed near synchronous orbit during disturbed periods and showed by means of a simple wire model that a dramatic increase of the current in the inner nightside magnetosphere must accompany the substorm growth phase. A recent detailed study by Fairfield *et al.* (1987) based on *AMPTE* magnetic field measurements also corroborates the concept of a thin intense tail current sheet deeply embedded into the inner nightside magnetosphere.

(2) Statistical studies of the average shape and position of the tail neutral sheet (Russell and Brody, 1967; Fairfield, 1980; Gosling *et al.*, 1986), as well as theoretical considerations (Voigt, 1984) have shown that for non-zero tilt angle ψ between the z_{GSM} axis and that of the Earth's dipole the current sheet undergoes a two-dimensional warping. Near the midnight meridian plane the warping results in a gradual departure of the current sheet from the dipole equatorial plane towards that parallel to the solar wind stream. This is accompanied by a bending of the sheet in the *YZ* projection in such a way that, for $\psi > 0$, the current surface

is raised above the GSM equatorial plane in the central tail region, whereas it is depressed below this plane near the tail flanks (and vice versa for $\psi < 0$).

(3) Still in early experiments it has been established that the inner edge of the plasma sheet encircles the Earth over a considerable interval of local time (Frank, 1970), and the current flow line pattern in this region should also exhibit an arched configuration, which is manifested in a relatively large value of the B_y-component of the magnetic field observed outside the current sheet in dawn and dusk sectors (Speiser and Ness, 1967; Fairfield *et al.*, 1987).

In our earlier works (Tsyganenko and Usmanov, 1982; Tsyganenko, 1987; to be referred to hereafter as Papers 1 and 2, respectively) no effects of the current sheet warping have been incorporated in the model; the influence of the geodipole tilt on the geometry of the tail currents was simulated by a transverse displacement of the sheet as a whole by $z_s = R_H \sin \psi$. The largest discrepancies arising due to inaccuracy of this assumption should be expected in the pre-dawn and post-dusk sectors near the flanks of the tail. An attempt has also been made in these works to take into account the above mentioned curvilinearity of the current flow lines in the near nightside magnetosphere by introducing the factor $f(y)$, which attenuates the B_x and B_z components towards dawn and dusk flanks. This modification led to a bending of the current flow lines in the necessary direction; however, a significant amount of the current escaped from the sheet due to a j_z component, as a natural consequence of initial simplifying assumption $B_y^T = 0$. In fact, this means that we are unable to extend the sheet-like current structure into the dawn and dusk sectors in the framework of the proposed quasi-two-dimensional tail model.

There are reasons to conclude that the above mentioned short-comings lead to discrepancies between the model and the average observed magnetic field distribution in the near nightside magnetosphere. The neglect of the effects of the current sheet warping should result in an overestimate of the sheet thickness. The lack of axial symmetry in the current flow line pattern at the nightside, manifested in the absence of B_y field component, must distort the distribution of B_z in the region $-10\ R_E \lesssim x_{GSM} \lesssim 0$. Indeed, a comparison of the spatial variation of B_z observed at geosynchronous orbit with that deduced from the Paper 2 model (Sergeev, private communication, 1987) has shown that the computed curves exhibit a double-humped shape at the nightside, whereas the *ATS*-1

spacecraft data, as a rule, yield a curve with a single minimum attained near midnight. This feature can be easily understood, taking into account that in most cases the inner edge of the current sheet in the Paper 2 model is located closer to the Earth than the geosynchronous orbit.

In this work a somewhat different approach to the modeling of the intramagnetospheric current system is developed, which takes into account all the above mentioned peculiarities of the observed tail current sheet geometry.

2. A MODEL OF AN AXIALLY SYMMETRIC CURRENT SHEET AND ITS MODIFICATION

First of all, let us consider a problem to find the vector potential induced by an infinitely thin axially symmetric current sheet with a given radial distribution of the transverse component of the magnetic field. In accordance with axial symmetry, we introduce a cylindrical coordinate system (ρ, φ, z) and assume the vector potential to have only one component $\mathbf{A} = \{0, A(\rho, z), 0\}$.

Due to the absence of currents outside the sheet, we have $\nabla \times \nabla \times \mathbf{A} = 0$ for $z \neq 0$, or

$$\frac{\partial}{\partial \rho}\left(\rho^{-1}\frac{\partial}{\partial \rho}(\rho A)\right) + \frac{\partial^2 A}{\partial z^2} = 0 \qquad (1)$$

with a boundary condition at the sheet plane $z = 0$

$$\rho^{-1}\frac{\partial}{\partial \rho}(\rho A(\rho, 0)) = B_z(\rho). \qquad (2)$$

Separating variables in equation (1), we obtain the general solution as

$$A(\rho, z) = \int_0^\infty C(K)\,e^{-K|z|}J_1(K\rho)K^{1/2}\,\mathrm{d}K \qquad (3)$$

where the function $C(K)$ is to be determined from the boundary condition (2). Substituting (3) into (2), we find

$$B_z(\rho) = \rho^{-1/2}\int_0^\infty KC(K)J_0(K\rho)(K\rho)^{1/2}\,\mathrm{d}K \qquad (4)$$

and, inverting the transformation (4) (Bateman and Erdelyi, 1954) we arrive at

$$KC(K) = \int_0^\infty \rho^{1/2}B_z(\rho)(K\rho)^{1/2}J_0(K\rho)\,\mathrm{d}\rho. \qquad (5)$$

Inserting in equation (5) any desirable distribution of $B_z(\rho)$, we can, in principle, find the weight function $C(K)$ which, being then substituted in equation (3), will give the vector potential $A(\rho, z)$.

Bearing in mind that our final purpose is to solve an inverse problem by means of a least squares fitting to an extended experimental data set, we have to restrict ourselves to a limited class of distributions $B_z(\rho)$, which not only have the appropriate behaviour but also lead to a relatively simple combination of analytical forms in the expression for $A(\rho, z)$. Perhaps, the most compact solution satisfying these requirements corresponds to the following distribution of B_z

$$B_z^{(1)}(\rho) \sim (a^2 + \rho^2)^{-1/2} \qquad (6)$$

which provides the maximal disturbance at the origin and decreases to zero by $\rho \to \infty$. Substituting equation (7) into equation (5) and then into equation (3) leads (Bateman and Erdelyi, 1954) to a vector potential

$$A^{(1)}(\rho, z) \sim \rho^{-1}\{[(a + |z|)^2 + \rho^2]^{1/2} - (a + |z|)\}. \qquad (7)$$

Taking derivatives of equation (7) by the parameter a, we obtain a set of independent solutions of equation (1), corresponding to progressively larger rates of decrease of B_z and the current density by $\rho \to \infty$. For our purpose it is enough to take the first and the second derivatives, which yield

$$A^{(2)}(\rho, z) = \frac{\partial A^{(1)}}{\partial a} \sim \rho^{-1}\left\{1 - \frac{a + |z|}{[(a + |z|)^2 + \rho^2]^{1/2}}\right\} \qquad (8)$$

and

$$A^{(3)}(\rho, z) = \frac{\partial A^{(2)}}{\partial a} \sim \rho[(a + |z|)^2 + \rho^2]^{-3/2} \qquad (9)$$

with the corresponding B_z distributions

$$B_z^{(2)}(\rho, 0) \sim (a^2 + \rho^2)^{-3/2}$$

and

$$B_z^{(3)}(\rho, 0) \sim (\rho^2 - 2a^2)(a^2 + \rho^2)^{-5/2}. \qquad (10)$$

Note that only the third solution, $A^{(3)}$, yields the current distribution $I(\rho)$ with a finite magnetic moment

$$M = (\pi/c)\int_0^\infty I(\rho)\rho^2 \, d\rho.$$

This can also be seen from the fact that the potential $A^{(3)}$ tends to that of a magnetic dipole by $\rho, z \to \infty$. It is also worth noting that $A^{(3)}$ bears a resemblance to

the vector potential of a model ring current introduced in Paper 1.*

Having thus derived a set of solutions for an infinitely thin disc-shaped current, let us extend them to the case of a distributed current sheet having a non-zero scale size of the volume current density profile in the transverse direction. To obtain the potentials corresponding to a sheet with a characteristic half-thickness scale D, no more is required than to remove the discontinuity in B_x at $z = 0$ caused by the kink of $|z|$ entering in equations (7–9). The simplest way to do that is to replace $|z|$ by $(z^2 + D^2)^{1/2}$. Strictly speaking, this modification of the vector potential gives rise to a non-zero current in the whole space outside the plane $z = 0$. However, as the direct calculation of $\nabla \times \nabla \times \mathbf{A}$ shows, the electric current density rapidly goes to zero (as $\sim z^{-2}$) for $z > D$, so that the layers between the planes $z = \pm D$ and $z = \pm 2D$ contain ≈ 75 and $\approx 95\%$ of the total current, respectively.

One more possible generalization can be obtained by assuming $D = D(\rho, \varphi)$ or $D = D(x, y)$, which enables us to model spatial variations in the current sheet thickness scale. The last statement is also not quite evident a priori, because the modified magnetic field structure is obtained here as a result of a formal generalization of the vector potential, rather than a solution of a direct problem starting from a properly modified electric current distribution. Therefore, we have to carry out an a posteriori verification of the effects that are expected to be obtained in the electric current pattern. Such a test computation has shown that the necessary modification of the current density distribution can indeed be clearly discernible in the $\mathbf{j} = (c/4\pi)\nabla \times \nabla \times \mathbf{A}$ plots. The only limitation here is that the spatial variation of D should be rather gradual, to avoid too large artificial currents outside the layer related to the non-constancy of D.

The next step is to replace the z coordinate in equations (7–9) by $z' = z - z_s$, where $z_s = z_s(\rho, \varphi)$ or $z_s = z_s(x, y)$ is a function defining the shape of the warped current sheet. In the magnetospheric model described below the function z_s also includes a parametric dependence on the geodipole tilt angle. Again, this modification of the vector potential can allow for only a smooth bending of the current sheet, since for $z_s \neq$ const an additional artificial current appears outside the sheet, proportional to the second derivatives of z_s, i.e. to the sheet curvature. The foregoing extension of the initially symmetric model does not violate the divergence condition $\nabla \cdot \mathbf{B} = 0$, because it is applied to the vector potential, rather than to the field $\mathbf{B}$. The only reservation here is that an arbitrary gauge is introduced instead of the Coulomb one.

---

* After the present work had been completed, I discovered the paper by Connerney et al. (1981), in which a similar approach is addressed in modeling the Jovian magnetodisc. A principal difference between that model and the present one consists in that Connerney et al. start from an explicit form of the current density distribution, whereas I impose the boundary condition by defining a B_z radial profile and then obtain a family of exact analytical solutions.
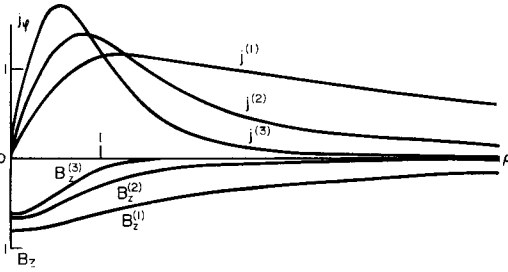
FIG. 1. PROFILES ILLUSTRATING THE DISTRIBUTION OF THE
VOLUME CURRENT DENSITY AND THE TRANSVERSE COMPONENT
OF THE MAGNETIC FIELD IN THE EQUATORIAL PLANE OF THE
AXIALLY SYMMETRIC MODEL CURRENT DISCS OF A FINITE
THICKNESS SCALE.
The characteristic radial scale length, a, and the transverse
half-thickness scale, D, equals 1.0 and 0.25, respectively.
Both j_φ and B_z are scaled in arbitrary units.

The magnetic field components B_ρ and B_z and then
the electric current volume density $\mathbf{j}$ can now be deter-
mined from the above derived vector potential. Figure
1 shows radial distributions of j_φ (in arbitrary units)
in the equatorial plane $z = 0$, corresponding to the
three finite-thickness disc models obtained from equa-
tions (7–9) with $a = 1$, $D = 0.25$ where no warping
or asymmetry effects had been introduced here. The
corresponding curves of $B_z(\rho, 0)$ are given below the
horizontal axis. Current densities reach the maximal
values at $\rho \sim a$ and decrease to zero by $\rho \to \infty$ with
markedly different rates, which is reflected in a differ-
ent characteristic broadness of the B_z profiles.

Making a linear combination of the potentials,
corresponding to $A^{(1)}$–$A^{(3)}$ in equations (7–9) with
different weight coefficients, scale lengths a and half-
thickness values D, it is possible to obtain a wide
variety of magnetic field models corresponding to the
finite-thickness warped disc-like current distributions.
They can be applied to represent the magnetospheric
configurations of Jupiter and Saturn. As it is shown
below, some further modification of the model allows
its application to the Earth's magnetosphere.

3. TERRESTRIAL MAGNETOSPHERE: THE RING CURRENT AND THE TAIL CURRENT SYSTEM

Based on the cumulative body of experimental evi-
dence referred to in Section 1, we can assume that the
ring current and the tail current form a united sheet-
like system in the near nightside magnetosphere, with
an arch-shaped configuration of the current flow lines.
At relatively small geocentric distances the current
sheet nearly coincides with the dipole equatorial plane
and gradually departs from it at larger distances,
approaching asymptotically a plane parallel to that of
the solar magnetospheric equator.

The model developed below is based on the vector
potential representation for the warped current disc
matched with the dipole equatorial plane near the
Earth. By this reason the solar magnetic coordinate
system (SM) will be used below in defining the current
sheet geometry and in the derivation of the
expressions for the magnetic field components. The
following function was chosen to describe the shape
of the nightside current sheet:

$$Z_s(x, y, \psi) = 0.5tg\psi(x + R_c - \sqrt{(x + R_c)^2 + 16})$$
$$- G\sin\psi \cdot y^4(y^4 + L_y^4)^{-1} \quad (11)$$

which contains two free parameters, R_c and G. The
former one is similar to the "hinging distance" (see
Paper 1 and references therein) and determines a
characteristic distance to a region, where the current
sheet warps and departs from the plane $Z_{SM} = 0$. The
latter parameter, G, specifies the degree of the trans-
verse bending of the current sheet. The quantity L_y in
the last term in equation (11) was set at a fixed value
$L_y = 10R_E$, in accordance with results of Fairfield
(1980) and Gosling et al. (1986). In Fig. 2 the shape
of the model current sheet is displayed, with $\psi = 30^\circ$,
$R_c = 8R_E$ and $G = 10R_E$.

The curves $j^{(1)}$ and $j^{(2)}$ in Fig. 1 provide a good fit
to a characteristic distribution of the current density
in the geomagnetotail plasma sheet (see Paper 2). It
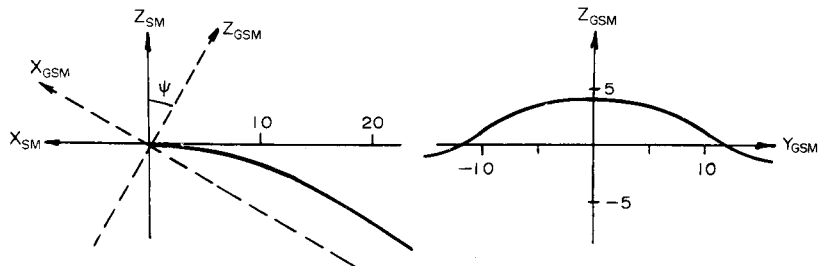is thus reasonable to choose the potentials in equa-

FIG. 2. ILLUSTRATING THE GEOMETRY OF THE WARPED MODEL CURRENT SHEET IN TWO CROSS-SECTIONS,
ACCORDING TO EQUATION (11), FOR $\psi = 30^\circ$, $R_c = 8 R_E$, $G = 10 R_E$, $L_y = 10 R_E$.

tions (7) and (8) as a basis for modeling the tail current system. However, the initial axis-symmetric model field [equations (7)–(9)] extends over all local times and therefore some modification is necessary to remove or re-distribute the current at the dayside and to confine the main part of the current sheet to the magnetotail domain. In the proposed model it is achieved, firstly, by a special choice of the function $D(x, y)$ defining the current sheet thickness profile. Namely, the sheet is supposed to become thicker towards the dayside and towards the flanks of the tail. Secondly, the vector potential of the disc is multiplied by a factor $W(x, y)$, which equals unity in the central tail region ($x \lesssim -10R_E$, $y \sim 0$) and smoothly drops off to zero towards subsolar magnetopause region, as well as for $|y| \to \infty$. As the direct computation of $\nabla \times \mathbf{B}$ has shown, this results in such a re-distribution of the initially axisymmetric current flow pattern, that both the total current and the gradient of the volume current density are depressed throughout the dayside magnetosphere. In the nightside region the current is localized within a thin sheet centered at the warped surface $z = z_s(x, y, \psi)$.

As for modeling the ring current contribution, it is the most appropriate to proceed from the potential $A^{(3)}$ in equation (9), since it provides the most localized current density profile with the highest rate of decrease towards larger distances. Possible effects of the day–night asymmetry are incorporated in the ring current model by allowing the current sheet thickness to be a function of X_{SM}, like in the tail sheet model.

The results of computation of the model parameters from the experimental data has shown, that for all model versions with $K_p < 4^-$ a small "island" with a slightly negative B_z of the order of $-(0.5 \pm 1.0)$ nT is obtained persistently in the central part of the nightside current sheet ($-16 \lesssim x_{GSM} \lesssim -20$, $|y_{GSM}| \lesssim 4$). A direct inspection of data in this region, as well as statistical results by Fairfield (1986), lead to a conclusion that it is, most likely, an artefact of the extreme sensitivity of the B_z component in the sheet to the details of the current density distribution along the tail (see also a discussion of difficulties of the current "slab" models in the paper of Stern, 1987). A point here is that the B_z experimental values in the equatorial region are relatively small and hence the least square values of the model parameters are determined mainly by the B_x distribution in the tail lobes. Another possible reason can be a relative sparsity of data between $x_{GSM} = -10$ and $x_{GSM} = -20$ (see Fig. 1 of Paper 2). These reversals of B_z can be eliminated by introducing an insignificant thickening of the current sheet in the tailward direction, centered near $x_{GSM} \sim -16\ R_E$.

Final expressions for the azimuthal component of

the vector potential corresponding to the tail current sheet (labeled by the index T) and the ring current (RC) are as follows:

$$A^{(T)} = \frac{\rho W(x, y)}{S_T + a_T + \xi_T}\left(C_1 + \frac{C_2}{S_T}\right)$$

$$A^{(RC)} = C_5 \rho S_{RC}^{-3} \tag{12}$$

where

$$W(x, y) = 0.5\left(1 - \frac{x - x_0}{[(x - x_0)^2 + D_x^2]^{1/2}}\right)$$
$$\times (1 + y^2/D_y^2)^{-1},$$

$$S_{T,RC} = \sqrt{\rho^2 + (a_{T,RC} + \xi_{T,RC})^2},$$

$$\xi_{T,RC} = \sqrt{z_r^2 + D_{T,RC}^2},$$

$$z_r = z - z_s(x, y, \psi),$$

$$D_T = D_0 + \delta y^2 + \gamma_T h_T(x) + \gamma_1 h_1(x),$$

$$D_{RC} = D_0 + \gamma_{RC} h_{RC}(x) + \gamma_1 h_1(x),$$

$$h_{T,RC} = 0.5[1 + x(x^2 + L_{T,RC}^2)^{-1/2}],$$

$$h_1 = 0.5\{1 + (x + 16)[(x + 16)^2 + 36]^{-1/2}\}. \tag{13}$$

From equation (12) the magnetic field components are easily obtained as follows

$$B_x^{(T)} = Q_T x z_r,$$

$$B_y^{(T)} = Q_T y z_r,$$

$$B_z^{(T)} = \frac{W(x, y)}{S_T}\left(C_1 + C_2 \frac{a_T + \xi_T}{S_T^2}\right) + \frac{x\frac{\partial W}{\partial x} + y\frac{\partial W}{\partial y}}{S_T + a_T + \xi_T}$$
$$\times (C_1 + C_2/S_T) + B_x^{(T)}\frac{\partial z_s}{\partial x} + B_y^{(T)}\frac{\partial z_s}{\partial y}$$
$$- Q_T D_T\left(x\frac{\partial D_T}{\partial x} + y\frac{\partial D_T}{\partial y}\right) \tag{14}$$

where

$$Q_T = \frac{W(x, y)}{\xi_T S_T}\left[\frac{C_1}{S_T + a_T + \xi_T} + \frac{C_2}{S_T^2}\right] \tag{15}$$

and

$$B_x^{(RC)} = Q_{RC} x z_r,$$

$$B_y^{(RC)} = Q_{RC} y z_r,$$

$$B_z^{(RC)} = C_5 \frac{2(a_{RC} + \xi_{RC})^2 - \rho^2}{S_{RC}^5} + B_x^{(RC)}\frac{\partial z_s}{\partial x}$$
$$+ B_y^{(RC)}\frac{\partial z_s}{\partial y} - Q_{RC} D_{RC} x\frac{\partial D_{RC}}{\partial x} \tag{16}$$

where

$$Q_{RC} = 3C_5 \xi_{RC}^{-1} S_{RC}^{-5}(a_{RC} + \xi_{RC}) \quad . \quad (17)$$

The coefficients C_1, C_2 and C_5 specify the contribution to the total magnetic field from three terms, corresponding to [equations (7)–(9)] and having different decrease rates in the limit $\rho \to \infty$. Among the non-linear parameters of the model are the following: a_T and a_{RC}, the radial scale lengths, which define the geocentric distance to the current density maxima; x_0, the coordinate defining the location of the region of steepest decrease of the "truncation factor" $W(x, y)$; D_x and D_y, the scale lengths corresponding to variations of $W(x, y)$ along x- and y-axes; D_0, the half-thickness of the current sheet in the central magnetotail region; γ_{RC} and γ_T, the increments of the current sheet thickness between the nightside and dayside regions; L_T and L_{RC}, the scale distances for the functions h_T and h_{RC}, varying monotonically between zero and unity; δ, the factor defining the rate of the tail current sheet thickening towards its flanks. The model also contains two non-linear parameters R_C and G, which define the shape of the warped current sheet given by equation (11). The additional term, $\gamma_1 h_1$ in the expressions for D_T and D_{RC} provides a gradual thickening of the sheet in the tailward direction beyond $x_{GSM} \sim -15 R_E$ and eliminate the above mentioned B_z reversals in the near magnetotail.

All these parameters were by no means treated as variable ones in fitting the model to the experimental data sets, but only those, which possess a sufficient degree of independence of each other. This means that variations of these parameters about their initial tentative values should induce an essentially different re-distribution of the model magnetic field. For example, it is *a priori* clear that changes in the parameters γ_T and γ_{RC} will not lead to a significant variation of the magnetic field in the nightside region, whereas at the dayside they yield nearly the same effects. By this reason one of them, γ_T, has been fixed, and the other, γ_{RC}, has been left as a free parameter. From similar *a priori* considerations, as well as from the obtained *a posteriori* estimates of the parameter errors and trends in their behaviour in the course of successive iterations, it was finally decided to fix the following parameters by the values: $L_y = 10$, $D_x = 13$, $L_{RC} = 5$, $L_T = 6.3$, $\gamma_T = 4$, $\delta = 0.01$, $\gamma_1 = 1$. The following parameters were retained as free variables: coefficients C_1, C_2, C_5 and the non-linear parameters a_T, a_{RC}, x_0, D_y, D_0, γ_{RC}, R_C, G.

It should be emphasized once again that the nightside current sheet in this model has no abrupt inner edge. As can be seen from Fig. 1, it rather penetrates inward up to a very close geocentric distance, the current density varying here linearly with r. In principle, by adding more terms of the type [equations (7)–(9)] to the vector potential, it is possible to suppress the current in the innermost extraterrestrial region or to simulate the eastward diamagnetic current at the inner boundary of the radiation belt. However, an attempt to include these details on the model did not lead to any successful results; the most likely reasons are as follows.

(1) A relatively high level of the "noise" in the data, which smears out any fine structure in the field distribution.

(2) A relatively low density of the data points in the low-altitude region of the magnetosphere with $4 \lesssim r \lesssim 5 R_E$ with the absence of measurements at closer distances.

4. CONTRIBUTION FROM THE MAGNETOSPHERIC BOUNDARY SOURCES

As pointed out in Paper 2, to obtain a correct distribution of both B_x and B_z in the model magnetospheric tail, it is necessary to incorporate the effects from the return current closing the central tail current sheet across the high-latitude magnetopause regions and enveloping the lobes. In the present model version these sources are simulated by a pair of planar current sheets parallel to the GSM equatorial plane and located at $z_c = +R_T$, with $R_T = 30 R_E$. The contribution from each sheet was represented by the vector potential of the $A^{(1)}$ type in equation (7) with a "truncation factor" $W_c(x, y)$ similar to that in the central sheet model. Since both sheets are located outside the modeling region, it is possible to make simplifying assumptions $a = 0$ and $D = 0$. In contrast with Paper 2, no constraint conditions have been imposed on the total current in both sheets, which would relate it to the total central sheet currents. Rather, it was assumed, that the contribution from the return current can be divided into two terms, symmetrical and antisymmetrical with respect to the dipole tilt angle, ψ. The first term represents the main part of the field corresponding to perpendicular geodipole orientation, and the second one models the effect of asymmetry between the northern and southern lobes arising due to the dipole tilt. Final expressions for the return current contribution are as follows:

$$B_{x,y,z}^{(c)} = C_3(F_{x,y,z}^+ + F_{x,y,z}^-) + C_4(F_{x,y,z}^+ - F_{x,y,z}^-)\sin\psi \quad (18)$$

where

$$\begin{Bmatrix} F_x^\pm \\ F_y^\pm \end{Bmatrix} = \pm \frac{W_c(x,y)}{S^\pm [S^\pm \pm (z \pm R_T)]} \times \begin{Bmatrix} x \\ y \end{Bmatrix},$$

$$F_z^\pm = \frac{W_c(x,y)}{S^\pm} + \left(x \frac{\partial W_c}{\partial x} + y \frac{\partial W_c}{\partial y} \right)$$

$$\times \frac{1}{S^\pm \pm (z \pm R_T)},$$

$$S^\pm = [(z \pm R_T)^2 + x^2 + y^2]^{1/2},$$

$$W_c(x,y) = 0.5 \left[1 - \frac{x - x_{0c}}{[(x - x_{0c})^2 + L_{xc}^2]^{1/2}} \right]$$

$$\times (1 + y^2/D_{yc}^2)^{-1}. \tag{19}$$

Note that x, y, z here are the solar-magnetospheric coordinates, rather than solar-magnetic ones, as in [equations (12)–(17)].

Due to a relatively small contribution of these sources to the total field, only coefficients C_3 and C_4 were assigned to be variable parameters. All the non-linear parameters were fixed at values $R_T = 30$, $x_{0c} = 4$, $L_{xc}^2 = 50$, $D_{yc} = 20$, chosen from *a priori* considerations and preliminary test runs.

Contribution from the Chapman–Ferraro currents at the magnetopause and that from the rest of intra-magnetospheric sources (including field-aligned currents) was chosen in the present model just the same as in the Paper 2 "truncated" version. By this reason, the corresponding expressions are reproduced below without detailed comments:

$$B_x^{(M)} = e^{x/\Delta x}[C_6 z \cos \psi + (C_7 + C_8 y^2 + C_9 z^2) \sin \psi],$$

$$B_y^{(M)} = e^{x/\Delta x}[C_{10} yz \cos \psi + (C_{11} y$$
$$+ C_{12} y^3 + C_{13} yz^2) \sin \psi],$$

$$B_z^{(M)} = e^{x/\Delta x}[(C_{14} + C_{15} y^2 + C_{16} z^2) \cos \psi$$
$$+ (C_{17}z + C_{18}zy^2 + C_{19}z^3) \sin \psi] \tag{20}$$

where Δx is a characteristic scale length along the Sun–Earth direction. The last four coefficients C_{16}–C_{19} are not independent, since they are expressed through the first ones in accordance with equation $\nabla \cdot \mathbf{B} = 0$. Hence, these terms yield 11 free parameters, namely, Δx and C_6–C_{15}.

5. RESULTS

5.1. *Analysis of the model parameters*

Numerical fitting of the model parameters to the measured magnetic field has been carried out by means of the same algorithms and using the same data, as in the Paper 2. Therefore, only a brief outline of the most important points is given below; the reader is referred to that work for details.

The merged spacecraft data set used as the experimental base for the modeling contains 36,682 vector averages of the magnetospheric field measured during the period from 1966 to 1980 aboard eight *IMP* and two *HEOS* satellites in the geocentric distance range from 4 to 70 R_E. Computations were carried out for a series of data subsets created by sorting out the measurements corresponding to selected intervals of the geomagnetic activity indices (K_p). In this work the same six data subsets have been used, as in the Paper 2 "long" model version, namely, $K_p = 0, 0^+$, $K_p = 1^-, 1, 1^+$, $K_p = 2^-, 2, 2^+$, $K_p = 3^-, 3, 3^+$, $K_p = 4^-, 4, 4^+$, and $K_p \geqslant 5^-$. The only difference is that in the earlier work a consolidation procedure had been applied to the second, third, and fourth subset, in order to reduce excessively large numbers of data points. Now it was decided to abandon this procedure; as a result, an insignificant increase in the average external field values occurred in these three subsets.

The model parameters listed in Section 3 were found for each data subset by means of an iterative algorithm incorporating a standard least squares technique for computing the linear parameters and the Newton–Lecam–Marquardt method for the non-linear ones. It was also possible to estimate the errors of the parameter values obtained, as well as to assess the degree of intercorrelation between them.

The calculated model parameters are listed in Table 1; the columns, from left to right, correspond to progressively larger values of the K_p index. As can be seen from the comparison of the present table with Table 1 of Paper 2, in four cases out of six we obtain a decrease of the r.m.s. residuals σ, the most pronounced changes being observed for the extremal values of the K_p-index (a decrease from 6.7 to 6.5 for $K_p = 0, 0^+$ and from 15.7 to 15.1 for $K_p \geqslant 5^-$). A slight increase occurred for the subsets with $K_p = 1^-, 1, 1^+$ and $K_p = 2^-, 2, 2^+$; note, however, that the $\langle B_e \rangle$ is also a little greater in this case, so that the "figure of merit" $\langle B_e \rangle / \sigma$ remains nearly the same. The attained improvement of the model, judging from the decrease of the over-all averages of the residual field, seems to be rather modest. However, we have to realize that, firstly, the predominant part of the σ is contributed by ineradicable residual "noise" in the data sets, caused by fluctuations in the solar wind pressure and a mixture of very different geophysical situations in the cumulative body of measurements taken at different times, rather than by an imperfection of the mathematical model. Secondly, the improvements described above of the model are related to a limited region of the near tail current sheet, containing a comparatively small part of the

Table 1

	$K_p = 0, 0^+$	$K_p = 1^-, 1, 1^+$	$K_p = 2^-, 2, 2^+$	$K_p = 3^-, 3, 3^+$	$K_p = 4^-, 4, 4^+$	$K_p \geqslant 5^-$
N	3975	9977	9848	7309	3723	1850
$\langle B_c \rangle$	15.49	19.06	21.71	25.48	28.58	32.88
σ	6.51	8.52	9.75	11.35	12.41	15.12
c_1	-98.72	-35.64	-77.45	-70.12	-162.5	-128.4
c_2	-10014	-12800	-14588	-16125	-15806	-16184
c_3	15.03	14.37	64.85	90.71	160.6	149.1
c_4	76.62	124.5	123.9	38.08	5.888	215.5
c_5	-10237	-13543	-16229	-19630	-27534	-36435
c_6	1.813	2.316	2.641	3.181	3.607	4.090
c_7	31.10	35.64	42.46	47.50	51.10	49.09
c_8	-0.07464	-0.0741	-0.07611	-0.1327	-0.1006	-0.0231
c_9	-0.07764	-0.1081	-0.1579	-0.1864	-0.1927	-0.1359
c_{10}	0.003303	0.003924	0.004078	0.01382	0.03353	0.01989
c_{11}	-1.129	-1.451	-1.391	-1.488	-1.392	-2.298
c_{12}	0.001663	0.00202	0.00153	0.002962	0.001594	0.004911
c_{13}	0.000988	0.00111	0.000727	0.000897	0.002439	0.003421
c_{14}	18.21	21.37	21.86	22.74	22.41	21.79
c_{15}	-0.03018	-0.04567	-0.04199	-0.04095	-0.04925	-0.05447
c_{16}	-0.03829	-0.05382	-0.06523	-0.09223	-0.1153	-0.1149
c_{17}	-0.1283	-0.1457	-0.6412	-1.059	-1.399	-0.2214
c_{18}	-0.001973	-0.002742	-0.000948	-0.001766	0.000716	-0.01355
c_{19}	0.000717	0.001244	0.002276	0.003034	0.002696	0.001185
Δx	24.74	22.33	20.90	18.64	18.31	19.48
a_{RC}	8.161	8.119	6.283	6.266	6.196	5.831
D_0	2.08	1.664	1.541	0.9351	0.7677	0.3325
γ_{RC}	-0.8799	0.9324	4.183	5.389	5.072	6.472
R_c	9.084	9.238	9.609	8.573	10.06	10.47
G	3.838	2.426	6.591	5.935	6.668	9.081
a_T	13.55	13.81	15.08	15.63	16.11	15.85
D_y	26.94	28.83	30.57	31.47	30.04	25.27
X_0	5.745	6.052	7.435	8.103	8.260	7.976

experimental data points. This leads to an additional attenuation of the visible effects in the σ values.

As can be seen from Table 1, the three coefficients C_1, C_2 and C_5, which define the current distribution in the central current sheet, show in general an orderly increase with the K_p-index. The coefficient C_1 corresponding to the most slowly varying part of the vector potential and current changes in a somewhat more chaotical manner, than C_2 and C_5 do, but the total model field shows in general a more regular dependence on K_p, since the fluctuations in its separate terms are approximately cancelled by each other. Note also that the most dramatic increase is observed in the coefficient C_5 corresponding to the most localized part of the central sheet current. Hence, the increase in the disturbance level is manifested in the increase of the tail current magnitude mainly in its innermost region, in accordance with earlier results (Paper 2, Fig. 5).

The coefficient C_3 defining the symmetric part of the closure current contribution also grows rapidly with K_p, but the amplitude of the antisymmetric term, C_4, exhibits a more complex behaviour. Nevertheless, the non-monotonic abrupt changes of this term are

also reduced by other terms in the total field; this is evident, for example, from a distinct correlation between the coefficients C_4 and C_{17}, corresponding to the terms with the same type of symmetry in the B_z component.

The coefficients C_6–C_{19} of the expansions in equation (20) have the same order of magnitude and reveal basically the same dependence on K_p, as the corresponding coefficients a_1–a_6 in the "truncated" model developed earlier (Paper 2, Table 2).

With regard to the non-linear parameters, the most conspicuous feature is a rapid monotonic decrease of the current sheet half-thickness D with increasing K_p, from $D \approx 2.1$ for $K_p = 0, 0^+$ up to $D \approx 0.3$ for $K_p \geqslant 5^-$. In order to clarify this result, note that the thinning of the model current sheet in the near magnetotail should, in principle, be manifested not only in a thinning of the B_x-component reversal region, but also in an increase of the magnitude of B_z depression in the whole region adjacent to the inner part of the current sheet. Since the density of our experimental data points in this region is rather low and the actual current sheet location in the Z direction can fluctuate

considerably from case to case, then we have to conclude that the obtained close and clear relationship between D and K_p, as well as such a small value of D for disturbed conditions are related mainly to the peculiarities of the B_z distribution, rather than to the extremely regular pattern of the B_x reversals.

The next feature of the current sheet geometry evident from Table 1 consists in a distinctly growing asymmetry between the dayside and nightside sector with increasing K_p. This asymmetry is defined by the parameter γ_{RC}, which appears to be slightly negative for $K_p = 0, 0^+$ and then grows almost monotonically up to ≈ 6.5 by $K_p \geqslant 5^-$. Therefore, thinning of the sheet at the nightside is accompanied by its considerable thickening at the dayside, with increasing disturbance level. The quantity a_{RC} defining the characteristic scale radius of the ring current also decreases monotonically, although within a rather limited range from ≈ 8.2 in very quiet up to ≈ 5.8 in the most disturbed conditions. A similar quantity a_T corresponding to the more slowly varying tail field terms shows a gradual increase with K_p, though also within a narrow interval between 13.6 and 15.9.

Of the two parameters, R_c and G, which determine the effects of the current sheet warping, only the last one exhibits a pronounced change, increasing from 3.8 to 9.1 with growing K_p. The former parameter, R_c, varies between 9.1 and 10.5. Thus, the influence of the disturbance level is mainly manifested in the degree of the transverse bending of the current sheet. Under quiet conditions the amplitude of diurnal and seasonal motion of the current sheet with respect to the GSM equatorial plane shows a relatively weak dependence on Y_{GSM}. During disturbed conditions the central part of the sheet oscillates with nearly the same amplitude, whereas towards the flanks the displacement tends to zero or even becomes negative. With regard to the parameter R_c, the observed lack of its dependence on K_p (in fact, R_c even grows slightly with K_p) is in obvious disagreement with our earlier results and other statistical studies (see Papers 1 and 2 and references therein), in which a clear trend of the "hinging distance" R_H to decrease with increasing K_p-index had been revealed. However, since planar current sheet models had been used in that work, the obtained R_H values correspond, in fact, to a spatially averaged amplitude of the current sheet transverse motion, which can be significantly less than the actual displacement near the midnight meridian, due to the bending of the sheet flanks towards the equatorial plane (note that typical R_H values obtained in Papers 1 and 2 are, indeed, by a factor 1.2–2.0 less than R_c values in the present study). The observed increase of G with K_p is equivalent to a decrease of the average

amplitude of the current sheet displacement manifested in a corresponding decrease of the "effective" hinging distance R_H reported in earlier papers.

The parameter x_0 defining the shift of the "truncation factor" $W(x, y)$ along the X-axis from the origin grows almost steadily with increasing K_p, which reflects a general enhancement of the intramagnetospheric currents in the dayside sector. The variation of the scale lengths Δx and D_y with K_p bears a qualitative resemblance with that obtained in Paper 1, though the numerical values are now significantly larger, due to the adopted modifications of the model functions and a more extended modeling region.

5.2. Model magnetic field distribution and field line configurations

A general comparison with the previous results of Papers 1 and 2 show that the most distinct changes in the model magnetic field distribution are observed in the nightside sector. It is just what was expected, since major improvements of the model concern the tail current and the nightside part of the ring current. The main result here is that a significantly more depressed field, and hence a more stretched force line pattern is obtained in the near magnetotail region for all K_p intervals, the most dramatic changes being observed for the highest level of disturbance.

Figure 3 gives a family of contours of constant B_z corresponding to the net contribution from all external model field sources in the plane $z_{GSM} = 0$, for three levels of disturbance, $K_p = 0, 0^+$, $K_p = 3^-, 3, 3^+$, and $K_p \geqslant 5^-$. The main tendency evident from these maps is a significant deepening of the B_z depression in the near-Earth region, the minima of ΔB being observed in all cases in the midnight sector at $x_{GSM} \approx -2.5$ R_E. However, real location of these minima and the corresponding ΔB_{min} values may be somewhat different from the model results, and the whole structure of external field and current distribution in the innermost near-Earth region can be significantly more complex; our data set coverage does not allow one to resolve finer details, since the experimental points are absent inside $r \sim 4$–5 R_E. Nevertheless, the obtained ΔB_{min} values seem to be in line with the existing measurements made at closer geocentric distances. According to the results of *AMPTE* magnetic field experiment (Fairfield *et al.*, 1987), a typical ΔB value inside $r \approx 5$ R_E in the near-equatorial nightside region is about $\Delta B \approx -80$ nT for $K_p > 3^+$. Since the number of data set points corresponding to a given K_p value drops off rapidly with increasing K_p, the main part of measurements taken by $K_p > 3^+$ falls into the interval $K_p = 4^-, 4, 4^+$. Computation using a present model with the corresponding set of parameters yields a
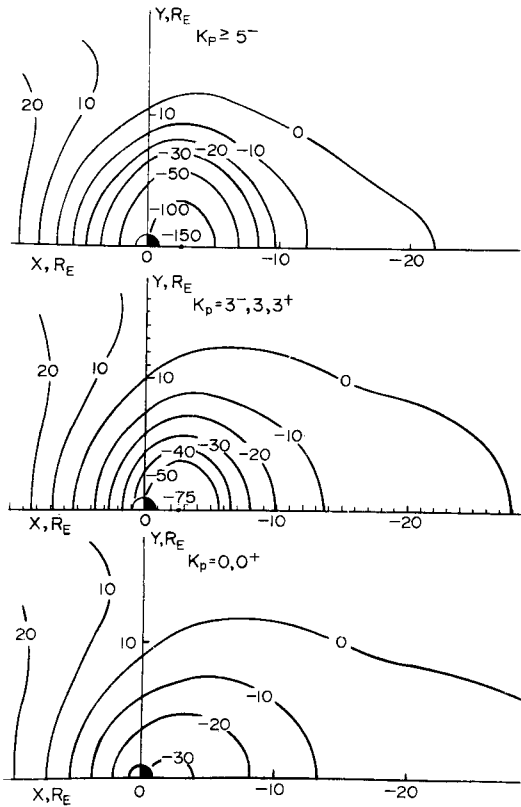
FIG. 3. THREE FAMILIES OF THE EQUAL INTENSITY CONTOURS OF THE EXTERNAL MODEL FIELD B_z IN THE GSM EQUATORIAL PLANE, FOR ZERO TILT ANGLE $\psi = 0$, CORRESPONDING TO THREE LEVELS OF DISTURBANCE.
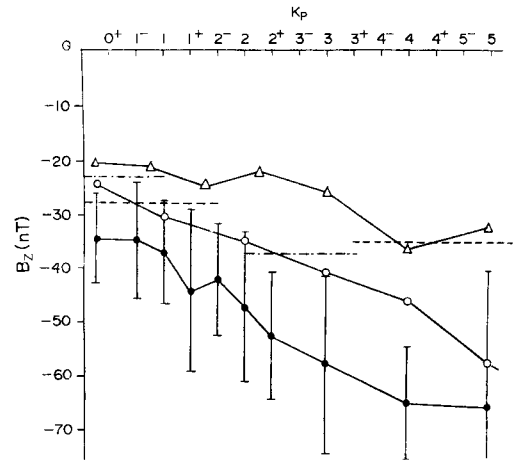

FIG. 4. PLOTS OF THE B_z COMPONENT OF THE EXTERNAL FIELD NEAR THE MIDNIGHT POINT OF THE GEOSYNCHRONOUS ORBIT VS K_p.

Open circles and triangles correspond to the present model and to the previous version (Tsyganenko, 1987), respectively. Solid circles, dashed line, and dashed–dotted line represent the average values obtained from ATS-1, $AMPTE$ and OGO-3, 5 spacecraft measurements, respectively.

value $\Delta B = -87$ nT for $x_{GSM} = -4\ R_E$; a minimal value $\Delta B_{min} \approx -103$ nT is attained at $x_{GSM} = -2.5\ R_E$, in good agreement with the above mentioned estimate by Fairfield *et al.* (1987).

Another tendency, also clearly seen in Fig. 3, is that a decrease in B_z occurs predominantly within the near tail domain with $X_{GSM} \gtrsim -12\ R_E$; at greater distances a slight increase of B_z with K_p is evident, manifested in an earthward shift of the $B_z = 0$ contour. This feature had also been noted in Paper 2 and was revealed in a number of preliminary test versions of the model, as well as in a direct inspection of the averages calculated from the experimental B_z values inside the plasma sheet region. Therefore, we are inclined to conclude that this is scarcely a modeling artefact but, rather, a manifestation of a real average increase of the tail magnetic flux connection through the neutral sheet during disturbed periods.

Figure 4 illustrates some results of comparison of the model field with the data from other spacecraft measurements, in the format of plots of the B_z component of the external field (geodipole contribution excluded) near the midnight point of the synchronous orbit ($r = 6.6\ R_E$) vs K_p-index. The open circles represent the B_z values computed using the present model and the triangles correspond to the "truncated" version of the Paper 2 model. The solid circles give the average B_z values measured on board the ATS-1 satellite in 1967 (a total of 232 hourly averages) and vertical bars show the corresponding r.m.s. deviation for each point. As seen from the plots, the present model yields a significantly more depressed field than that of Paper 2, but the ATS-1 curve is still ~ 10 nT lower. What is the cause of such a discrepancy, remains yet unclear, but we have to bear in mind that the H-component values in the ATS-1 data set were initially corrected by $\Delta H = -20$ nT, with a purpose to eliminate a positive bias mentioned in the work by Coleman and McPherron (1976) and related to uncertainties in evaluating the spacecraft magnetic field. The value of this additive correction had been specified, in particular, on the basis of our earlier work (Sergeev *et al.*, 1983), in which it was shown that the observed latitude Λ_i of the isotropic precipitation boundary for energtic protons show a very good correlation with the H_{ATS} measured at the midnight segment of the ATS-1 orbit. The correction of $\Delta H \approx -20$ nT appeared necessary to obtain the best fit of the experimental dependence of Λ_i on H_{ATS} to that

obtained from calculations of the latitudes of the non-adiabatic particle scattering boundaries, based on the Paper 1 magnetic field model. Thus, the above estimate for ΔH is model-dependent and hence may well be in error of ~ 10 nT.

Dashed and dashed-dotted lines in Fig. 4 represent the results of the *AMPTE* (Fairfield *et al.*, 1987) and *OGO* (Sugiura and Poros, 1973) measurements at $X \approx -6.6\ R_E$, respectively. For small K_p values the present model shows a good agreement with the data, while for $K_p > 3^+$ it provides a more depressed B_z, than that observed by the spacecraft.

It is also of much interest to use the statistical results by Lin and Barfield (1984) on the local time dependence of the measured average inclination angles at the geosynchronous orbit as an independent experimental test for our model. For this purpose the average values of the inclination angle, I, have been computed over the 12-month period for every hour of local time at the position of *GOES*-2 spacecraft, using the model distribuiton of the external magnetic field for three levels of the K_p-index, namely, $K_p = 1^-, 1, 1^+$, $K_p = 3^-, 3, 3^+$, and $K_p \geqslant 5^-$, These intervals of K_p most closely correspond to those chosen by Lin and Barfield (respectively, 0–2, 2–4 and 4–9) and, hence, are the most appropriate for comparison. Three panels of Fig. 5, from the bottom to the top, display the inclination dependence on the local time in the same format as in Fig. 6 of the paper by Lin and Barfield (1984), for the progressively higher levels of the K_p-index. The upper histograms in all three panels show the experimental results of *GOES* measurements taken directly from Fig. 6 of Lin and Barfield (1984). Smooth curves represent the modeling results. The dotted curves in the top and bottom panels correspond to the Mead and Fairfield (1975) model (taken from Fig. 7 of Lin and Barfield, 1984). The broken lines were obtained from the Paper 2 model, showing a better agreement with the *GOES* histograms. The best results are given by the present model (solid curves), which predicts the inclination angles near midnight much closer to the experimental values. However, there still remains a disagreement in that the all model curves lie below the *GOES* histograms. The largest discrepancies of about $15°$ correspond to the highest level of geomagnetic disturbance (upper panel) and are localized in the evening sector, showing a significant dawn–dusk asymmetry of the field line stretching, which is much smaller for a moderately disturbed magnetosphere and almost completely vanishes for the lowest activity interval $K_p = 0$–2.

As follows from Figs 4 and 5, the present model provides an improved representation of the geo-
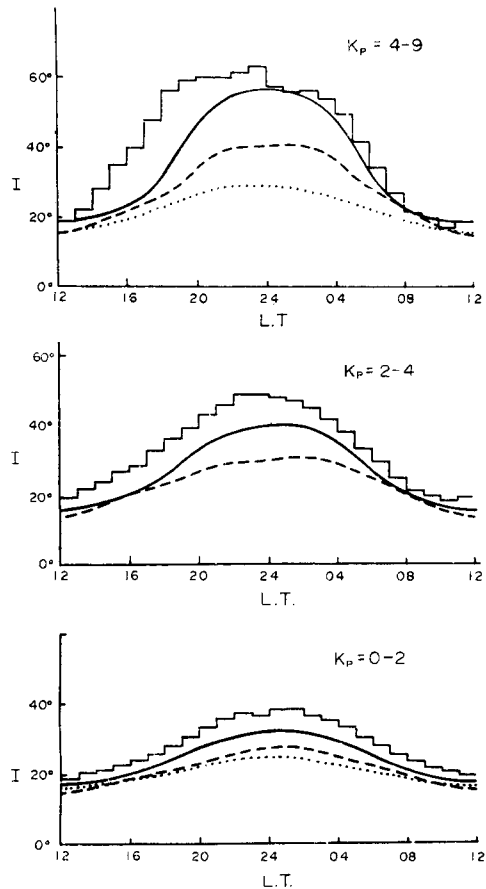

FIG. 5. COMPARISON OF THE INCLINATION ANGLES MEASURED BY *GOES*-2 SPACECRAFT (LIN AND BARFIELD, 1984) WITH THOSE PREDICTED BY THREE MODELS FOR DIFFERENT LOCAL TIMES.

Three panels, from the bottom to the top, correspond to progressively higher K_p levels. The upper histograms in each panel show the average distributions of the inclination angle measured by *GOES*-2 (radial distance $r \approx 6.6\ R_E$, dipole latitude $\varphi = 9.6°$) vs local time. Dotted lines, broken lines, and smooth solid lines correspond to the Mead–Fairfield (1975) model, the model by Tsyganenko (1987), and the present model, respectively.

magnetic field in the low-latitude nightside magnetosphere, despite the improvements being hardly visible in the overall r.m.s. residuals.

Figure 6 shows a family of the contours of constant volume density of electric current computed from the model magnetic field as $\mathbf{j} = (c/4\pi)\nabla \times \mathbf{B}$ in the midday–midnight meridian plane. The pattern corresponds to the moderately disturbed conditions $(K_p = 4^-, 4, 4^+)$ with the geodipole tilt angle close to its maximal value $\psi = 34.4°$, and clearly displays the expected warping of the tail current sheet. A small

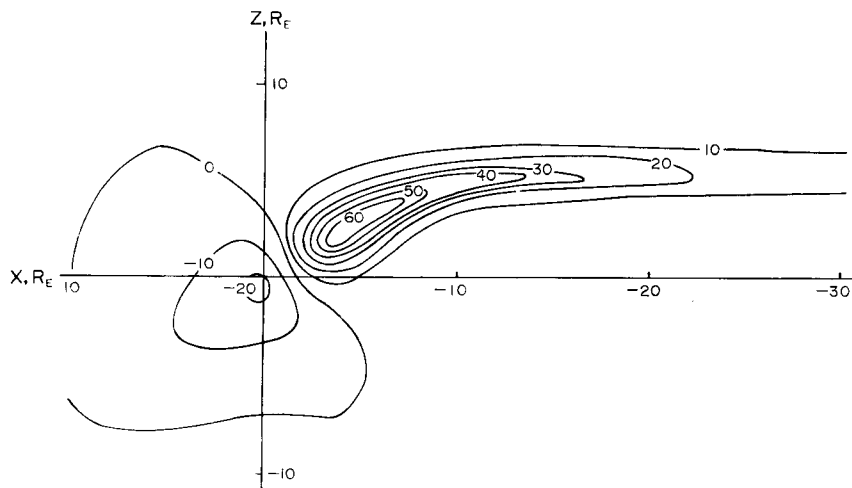FIG. 6. A FAMILY OF CONTOURS j_y = CONST IN THE MIDDAY–MIDNIGHT MERIDIAN PLANE, OBTAINED BY A DIRECT COMPUTATION OF $\nabla \times \mathbf{B}$ FOR THE MODERATELY DISTURBED SET OF THE MODEL PARAMETERS ($K_p = 4^-, 4, 4^+$) AND $\psi = 34.4°$.
The lines are labeled in units 10^{-10} A·m^{-2}. Note the warping of the current sheet and a significant day–night asymmetry of the current density distribution. The return current layers located at $z = \pm 30\ R_E$ lie outside the frame of this picture.

residual current density outside the central sheet region is the order of [equations (1)–(2)]·10^{-10} A·m^{-2} and is induced partly by terms in equation (20), since we have not imposed on them the condition $\nabla \times \mathbf{B} = 0$. A similar pattern of the j_y distribution in the tail cross-section at $X_{GSM} = -10\ R_E$ also reveals the expected warping of the model current sheet in the YZ-plane, as shown in Fig. 7. Two layers of return currents located at $Z_{GSM} = +30\ R_E$ are not shown,

being outside the frames of the figure, but it is just there, that the most part of the equatorial current is closed.

Figures 8–12 display the model field line configurations for several K_p intervals. As already noted above, the model shows significantly more stretched field lines at the nightside, in comparison with earlier model versions. Thus, for the highest disturbancy level with $K_p \geqslant 5^-$, the line starting at $66°$ dipole latitude
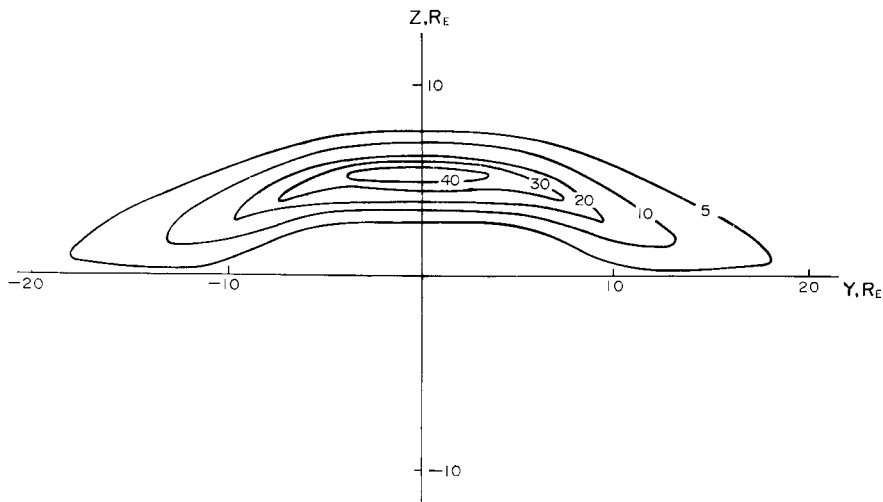

FIG. 7. A FAMILY OF CONTOURS OF j_y = CONST IN THE MAGNETOTAIL CROSS-SECTION $X_{GSM} = -10\ R_E$, SHOWING THE WARPING EFFECTS IN THE YZ PLANE.
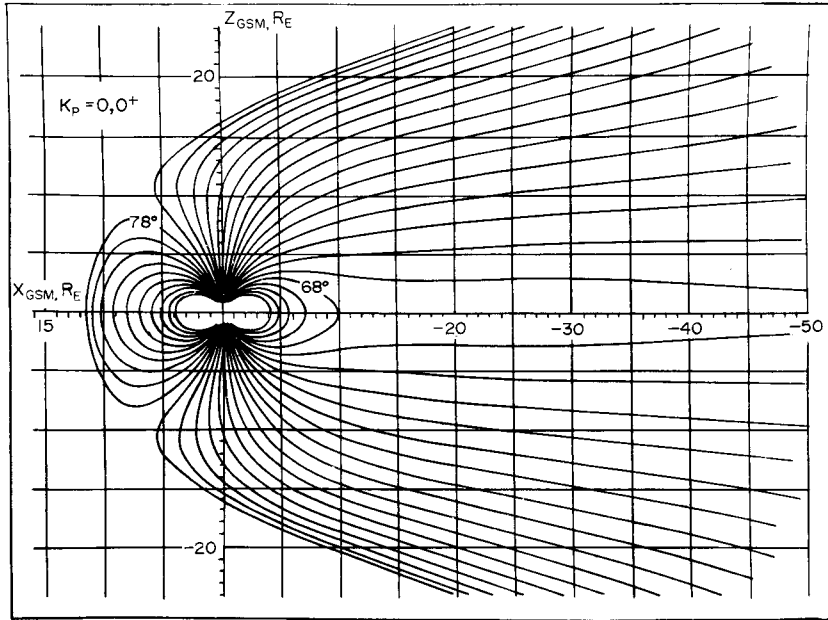
FIG. 8. FIELD LINE PATTERN IN THE NOON–MIDNIGHT MERIDIAN PLANE, CORRESPONDING TO VERY QUIET CONDITIONS ($K_p = 0, 0^+$).
Field lines start from Earth at latitudes 2° apart, beginning from 60°.
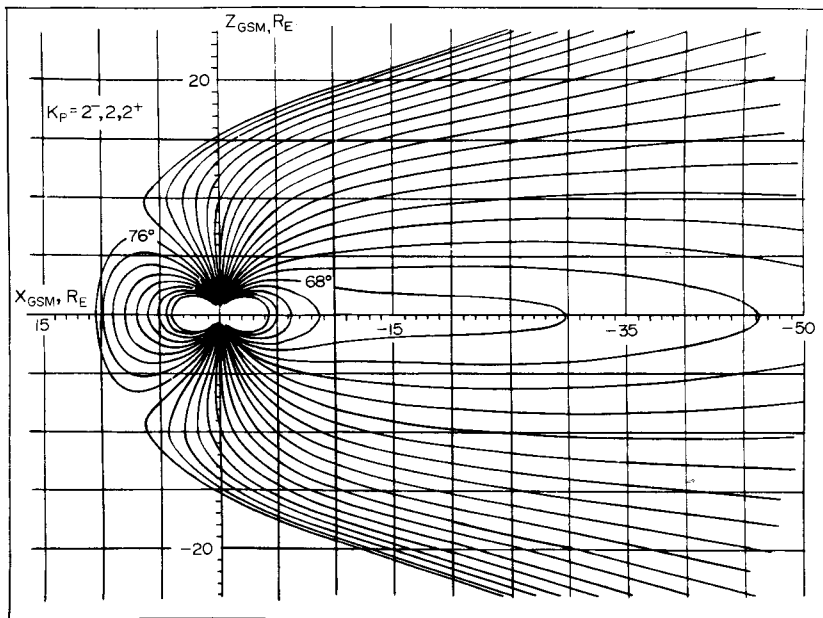

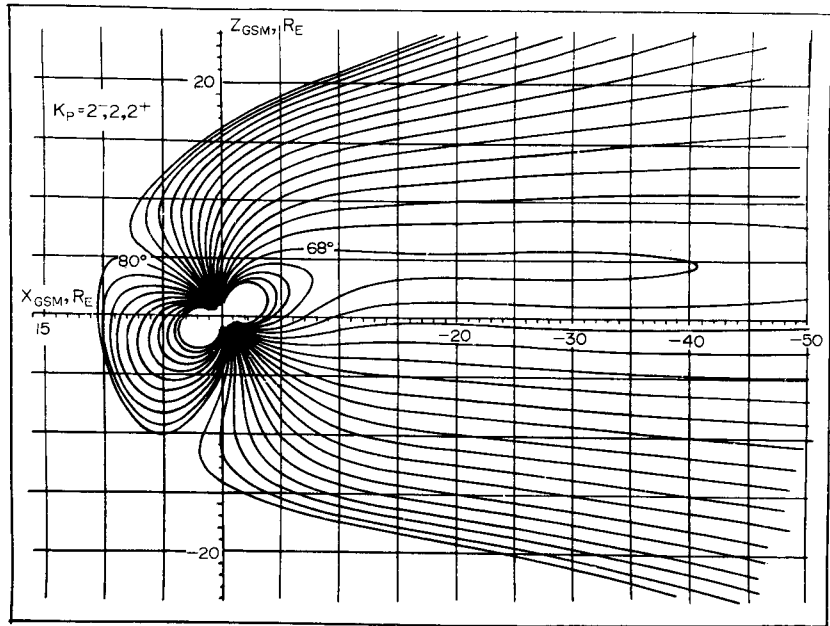FIG. 9. FIELD LINE PATTERN FOR AVERAGE QUIET CONDITIONS ($K_p = 2^-, 2, 2^+$).

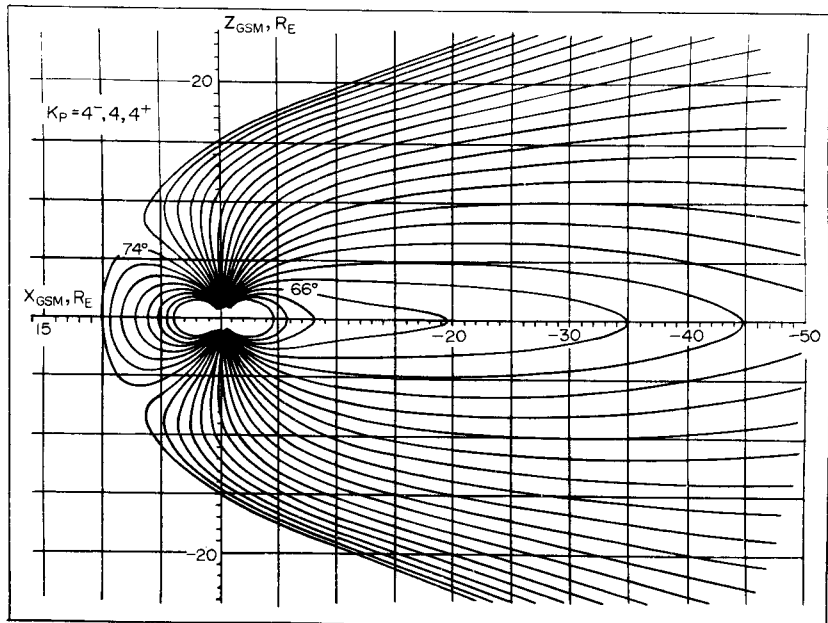FIG. 10. THE SAME, AS IN FIG. 9, FOR A TILTED GEODIPOLE WITH $\psi = 30°$.

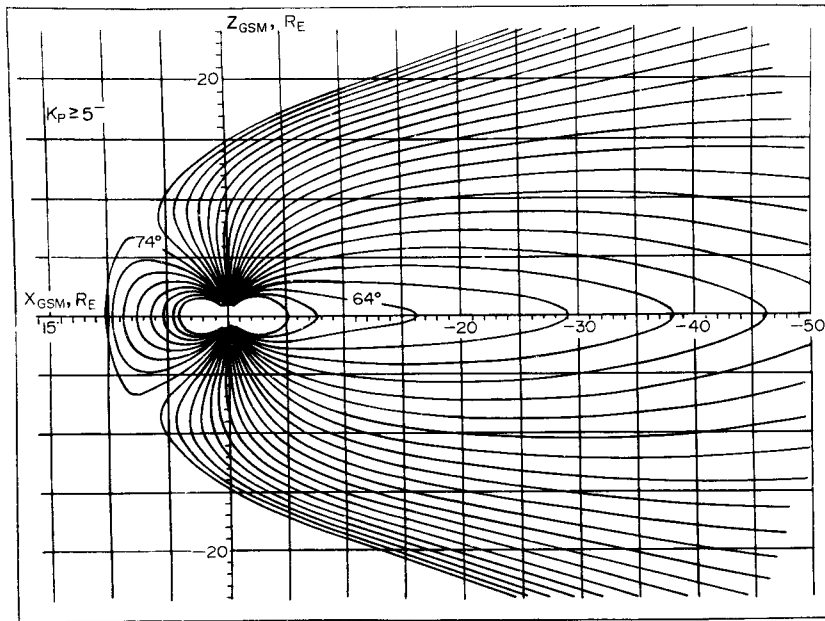FIG. 11. FIELD LINE PATTERN FOR A DISTURBED MAGNETOSPHERE ($K_p = 4^-, 4, 4^+$).

FIG. 12. FIELD LINE PATTERN FOR A STRONGLY DISTURBED MAGNETOSPHERE ($K_p \geqslant 5^-$).

from the Earth has its equatorial crossing point at $r_e = 30\ R_E$, while in the previous model we obtained ~ 3 times lesser r_e for the same K_p conditions.

As a final remark, it should be emphasized once again that the average configuration of the tail field lines crossing the plasma sheet and their mapping onto the Earth's surface is very sensitive to the details of the current distribution. In view of a relatively low density of the data points in the near-Earth region and at low latitudes in the near magnetotail, further work in this direction should be done, based on extended data sets.

REFERENCES

Bateman, H. and Erdelyi, A. (1954) Tables of Integral Transforms. McGraw-Hill, Maidenhead, U.K.
Coleman, P. J. and McPherron, R. L. (1976) Substorm observations of magnetic perturbations and ULF waves at synchronous orbit by ATS-1 and ATS-6, in Scientific Satellite Program during the International Magnetospheric Study (Edited by Knott, K. and Battrick, B.), pp. 345–365. D. Reidel, Dordrecht.
Connerney, J. E. P., Acuna, M. H. and Ness, N. F. (1981) Modeling the Jovian current sheet and inner magnetosphere. J. geophys. Res. 86, 8370.
Fairfield, D. H. (1980) A statistical determination of the shape and position of the geomagnetic neutral sheet. J. geophys. Res. 85, 775.
Fairfield, D. H. (1986) The magnetic field of the equatorial magnetotail from 10 to 40 R_E. J. geophys. Res. 91, 4238.
Fairfield, D. H., Acuna, M. H., Zanetti, L. J. and Potemra, T. A. (1987) The magnetic field of the equatorial magnetotail: AMPTE/CCE observation at $R = 8.8\ R_E$. J. geophys. Res. 92, 7432.
Frank, L. A. (1970) Plasma in the Earth's polar magnetosphere. J. geophys. Res. 76, 5202.
Gosling, J. T., McComas, D. J., Thomsen, M. F., Bame, S. J. and Russell, C. T. (1986) The warped neutral sheet and plasma sheet in the near-Earth geomagnetic tail. J. geophys. Res. 91, 7093.
Hedgecock, P. C. and Thomas, B. T. (1975) HEOS observations of the configuration of the magnetosphere. Geophys. J. R. astr. Soc. 41, 391.
Kaufman, R. L. (1987) Substorm currents: growth phase and onset. J. geophys. Res. 92, 7471.
Lin, C. S. and Barfield, J. N. (1984) Magnetic field inclination angle at geosynchronous orbit. Planet. Space Sci. 32, 1283.
Russell, C. T. and Brody, K. I. (1967) Some remarks on the position and shape of the neutral sheet. J. geophys. Res. 72, 6104.
Sergeev, V. A., Sazhina, E. M., Tsyganenko, N. A., Lundblad, J. Å. and Søraas, F. (1983) Pitch-angle scattering of energetic protons in the magnetotail current sheet as the dominant source of their isotropic precipitation into the nightside ionosphere. Planet. Space Sci. 31, 1147.
Speiser, T. W. and Ness, N. F. (1967) The neutral sheet in

the geomagnetic tail: its motion, equivalent currents and field line connection through it. *J. geophys. Res.* **72**, 131.

Stern, D. P. (1987) Tail modeling in a stretched magnetosphere—1. Methods and transformation. *J. geophys. Res.* **92**, 4437.

Sugiura, M. (1972) Equatorial current sheet in the magnetosphere. *J. geophys. Res.* **77**, 6013.

Sugiura, M. and Poros, D. J. (1973) A magnetospheric field model incorporating the *OGO* 3 and 5 magnetic field observations. *Planet. Space Sci.* **21**, 1763.

Tsyganenko, N. A. and Usmanov, A. V. (1982) Determination of the magnetospheric current system parameters and development of experimental geomagnetic field models based on data from *IMP* and *HEOS* satellites. *Planet. Space Sci.* **30**, 985.

Tsyganenko, N. A. (1987) Global quantitative models of the geomagnetic field in the cislunar magnetosphere for different disturbance levels. *Planet. Space Sci.* **35**, 1347.

Voigt, G.-H. (1984) The shape and position of the plasma sheet in Earth's magnetotail. *J. geophys. Res.* **89**, 2169.